Refinement effect of TiC on ferrite by molecular statics/dynamics simulations and first-principles calculations

Sha Liu [a], Yukui Gao [b], Zhijie Wang [a], Zhijun Shi [a], Yefei Zhou [a, c], **, Xuejun Ren [d], Qingxiang Yang [a], *

a State Key Laboratory of Metastable Materials Science & Technology, Yanshan University, Qinhuangdao, 066004, PR China
b School of Aerospace Engineering and Applied Mechanics, Tongji University, Shanghai, 200092, PR China
c College of Mechanical Engineering, Yanshan University, Qinhuangdao, 066004, PR China
d School of Engineering, Liverpool John Moores University, Liverpool, L3 3AF, UK

Abstract

The refinement mechanism of ferrite with TiC was investigated by molecular statics/dynamics and first principles. Ferrite is simplified as bcc-Fe model in this paper. The lattice parameters of bcc-Fe and TiC were optimized firstly. The works of adhesion and interfacial energies of bcc-Fe/TiC interfaces were calculated by molecular statics. The interfacial electronic structures were analyzed by first-principles. The solid-liquid interfacial energy of bcc-Fe is calculated by molecular dynamics. Results show that lattice parameters of bcc-Fe and TiC are a ¼ 2.87 Å and a ¼ 4.42 Å respectively. According to atomic stacking modes, three kinds of bcc-Fe/TiC interfaces were constructed. Their works of adhesion are 4.13 J/m2 (type-1), 1.01 J/m2 (type-2) and 3.41 J/m2 (type-3). Their interfacial energies are 0.29 J/m2 (type-1), 3.41 J/m2 (type-2) and 1.02 J/m2 (type-3). The type-1 interface is combined by FeeC polar covalent/ionic bonds. Type-2 interface is combined by FeeTi metallic bonds. Type-3 interface is combined by FeeC polar covalent/ionic bonds and FeeTi metallic bonds. The solid-liquid interfacial energy of bcc-Fe is 0.36 J/m2. Based on the classical nucleation theory, the interfacial energy of type-1 interface is lower than the solid-liquid interfacial energy of bcc-Fe, which means TiC can act as the heterogeneous nucleus of
bcc-Fe and thereby refines it.

1. Introduction

Ferritic stainless steel is noted for its excellent stress corrosion cracking resistance, good plasticity and toughness, high thermal conductivity and small linear expansion, which has been widely applied as corrosion resistant material in the modern industries [1].Furthermore, it is characterized of lower cost by comparison with austenite stainless steel, which makes it good substitute for austenite stainless steel. However, its low strength cannot meet the high requirement for mechanical properties, which restricts its widespread application [2]. Therefore, it has been noticed to improve the strength of ferritic stainless steel.

Nowadays, a lot of strengthening methods have been put forward, such as solid-solution strengthening, distortion strengthening, fine-grain strengthening and deposition strengthening [3-6]. Among them, the fine-grain strengthening method has attracted greatest attention for the improvement in strength and toughness of alloys simultaneously [7]. Z.W. Yu et al. [8] studied the grain size effect on magnesium-manganese alloy, and found that the ultra-fine grained alloy shows superior elongation and outstanding yield strength. M. Samaee et al. [9] found that the strength and ductility of AA6063 aluminum alloy are simultaneously improved by refining grain size. Recently, that ferrite can be refined by TiC, NbC and so on has been reported largely. The refinement is mainly ascribed to the heterogeneous nucleus effect and grain-growth-inhibiting effect [10-13]. Y. Kang et al. [14] studied the effect of Ti contents on the grain size and mechanical properties of UNS S44100 ferritic stainless steel, and the results show that the

average grain sizes of the as-cast specimens decrease obviously with increasing Ti content due to the increasing number of TiC precipitates. The similar effect of Nb contents on the grain size and mechanical properties of 18 wt%Cr ferritic stainless steel has also been proved, which is ascribed to NbC precipitates [15].

Ferrite solidifies directly from the liquid during the solidification
of ferritic stainless steel. According to the classical nucleation theory, foreign particles such as TiC can act as the heterogeneous nucleus only if the interfacial energy between TiC and ferrite is smaller than the solid-liquid interfacial energy of ferrite in homogeneous nucleation circumstance [16]. However, up to now, it is impossible to measure precisely the solid-liquid interfacial energy of ferrite by experiment. Therefore, it is difficult to explain the refinement mechanism of ferrite with TiC theoretically by experiment. Nowadays, first-principles calculation and molecular statics/dynamics simulation, which are of high accuracy, appeal much attention to the study on interfacial behaviors [17-19]. First principles calculation based on density functional theory raises concern for its insight into interfacial electronic structures. S.X. Jin et al. [20] calculated the interfacial electronic structure between TaN and ReB2, and found that strong covalent bonds are formed between B atoms and N atoms, which make TaN and ReB2 to combine together. J. Li et al. [21] analyzed the PDOS (partial densities of states) of Al/A13Ti interface and found the bonding between Al and A13Ti are AleAl metallic bonds and AleTi covalent bonds.
Molecular statics/dynamics simulation raises concern forthe insight into interfacial energy. A.C. Silva et al. [22] calculated the interfacial energy between g-Ni3Al and g-Ni by using molecular statics and found that the interfacial energy strongly depends on the composition of g-Ni. Y. Shibuta et al. [23] investigated the nucleation and solidification of the undercooled iron melt by using molecular dynamics, which successfully links the empirical interpretation in metallurgy with the atomistic behavior of nucleation and solidification. However, the refinement mechanism of ferrite with foreign particles by first-principles calculation and molecular statics/dynamics simulation has never been reported.

In this paper, the study object is ferrite with TiC. The interfacial energies between ferrite and TiC were calculated by molecular statics. The interfacial electronic structures were analyzed by first principles. Then the solid-liquid interfacial energy of ferrite in homogeneous nucleation circumstance was calculated by molecular dynamics. Finally, the refinement mechanism of ferrite with TiC was revealed.

2.1. Model facilitation
Ferrite is the solid solution of bcc-Fe with C atoms occupying the octahedral sites. The maximum solubility of C atoms at room temperature is 0.0008 wt%. Because of its low solubility, bcc-Fe model is frequently utilized to supplant ferrite in computations and simulations [24,25]. Therefore, bcc-Fe model was also utilized as ferrite in the present work.

2.2. Molecular statics
The molecular statics of bcc-Fe/TiC interfaces were fulfilled by using the Large-scale Atomic-molecular Massively Parallel Simulator (LAMMPS) based on the steepest descent algorithm. The systems in molecular statics always contain thousands to millions of atoms. The small difference in atomic energy can lead to quite different results, so the determination of the optimal lattice parameters is particularly important. Therefore, the lattice parameters of bcc-Fe and TiC were optimized firstly. After then, bcc-Fe/TiC interfaces were constructed and the works of adhesion and interfacial energies were calculated.

In the calculation process, the 2NN MEAM (second nearest nearest neighbour modified embedded atom method) [26-28] potential was applied to describe all the interactions of Fe, Ti and C atoms, in which the total energy E of the system is given as follow:

$$E = \sum_i \left\{ F_i(\rho_i) + \frac{1}{2} \sum_{i \neq j} S_{ij} \emptyset_{ij}(r_{ij}) \right\} \qquad (1)$$

where Fi is the embedding energy for atom i embedded in a background electron density ri; Sij is the screening function; Øij is the pair interaction between atoms i and j; rij is the distance between atoms i and j.

In the original MEAM potential, only the first nearest-neighbor interactions are considered by using a strong Sij. While in the 2NN MEAM potential, the second nearest-neighbor interactions have been put into consideration by adjusting Sij.

2.3. First-principles

The interfacial electronic structures of bcc-Fe/TiC interfaces were fulfilled by using the density functional theory as implemented in the Cambridge Sequential Total Energy Package (CASTEP). The exchange-correlation energy was described by the generalized gradient approximation (GGA). The plane-wave cutoff energies were 350eV and the Brillouin zone samplings were performed using 4x4x1 Monkhorst-Pack.

2.4. Molecular dynamics

The molecular dynamics simulation of bcc-Fe solid-liquid interfacial energy was also fulfilled by using LAMMPS. Firstly, the melting point of bcc-Fe was calculated. After then, the melting conditions of bcc-Fe embryos with different critical radii were simulated and the solid-liquid interfacial energy of bcc-Fe was calculated based on the classical nucleation theory. In the simulation process, the interaction of Fe atoms was described by the EAM (embedded atom method) potential developed specially for crystalline and liquid iron [29]. The total energy E of the system is given as follow:

$$E = \sum_i F_i(\rho_i) + \sum_i \sum_j \emptyset_{ij}(r_{ij}) \qquad (2)$$

where Fi is the embedding energy for atom i embedded in a background electron density ri; Øij is the pair interaction between atoms i and j; r_{ij} is the distance between atoms i and j.

3. Results and discussion

3.1. Lattice parameter

Crystal models of bcc-Fe with various lattice parameters (namely the values of a) are built, and they are fully relaxed by molecular statics. The relationship of equilibrium energies versus lattice parameters is displayed in Fig. 1a. The average atom energy is the lowest when a ¼ 2.87 Å, which indicates the crystal structure is most stable hereby. The lattice parameter is very close to the value (2.866 Å) in literature [30] with only 0.14% deviation. In the same way, the relationship of equilibrium energies versus lattice parameters of TiC (NaCl-type structure) is displayed in Fig. 1b. The average atom energy is the lowest when a ¼ 4.42 Å, which indicates the crystal structure is most stable hereby. The lattice parameter is only of 2.08% deviation from the value (a ¼ 4.33 Å) in literature [31]. Therefore, the subsequent simulations of bcc-Fe and TiC were fulfilled with these lattice parameters.

3.2. Interfacial energy of bcc-Fe/TiC

3.2.1. Interfacial relationship
There exists a well-known coherent interface between bcc-Fe and TiC with Baker-Nutting (BeN) orientation relationship
[32-36], that is:

$$\{001\}_{bcc-Fe}//\{001\}_{TiC}, \ 100_{bcc-Fe}//110_{TiC} \qquad (3)$$

According to the BeN relationship, there are three different types of bcc-Fe/TiC interfaces, which are: i) Fe atoms are just above C atoms (type-1); ii) Fe atoms are just above Ti atoms (type-2); iii) Fe atoms are just above the middle of adjacent two Ti atoms or C atoms (type-3). The three types of bcc-Fe/TiC interfaces are schematically displayed in Fig. 2.

3.2.2. Work of adhesion and interfacial energy
According to literature [37], the interfacial energy can be obtained by computing the total energy of a system that involves a bcc-Fe/TiC interface and the total energies of individual bcc-Fe and TiC systems of the same number of atoms as those in the interfacial system. Three bcc-Fe/TiC interfacial models are constructed based on the orientation relationship in Fig. 2, which are shown in Fig. 3. Because TiC precipitates firstly, the lattice parameter of TiC is set as the object of reference and that of bcc-Fe is changed accordingly. The lattice misfit between TiC and bcc-Fe with BeN orientation relationship is 8.1%. In order to remove any surface effects, three dimensional periodic boundary condition is applied, so two interfaces are involved into each model, which are marked by the arrows. To make the atomic stacking modes of the two interfaces in each model exactly the same, the upper and lower surfaces of bcc-Fe or TiC should be the same. The bcc-Fe/TiC interfacial models are of 4100 Fe atoms, 2100 Ti atoms and 2100 C atoms with the longest dimension (z-direction) perpendicular to the interfaces. The total energies of the interfacial models are calculated by molecular statics allowing full relaxations of atomic positions and model dimensions. While for the total energies of individual bcc-Fe and TiC models, the molecular statics merely allows full relaxations on the direction perpendicular to the interfaces but maintain the same lattice parameters as the interfacial models in two directions parallel to the interfaces. The interfacial energy g is given as follow:

$$\gamma = \left[E_{bcc-Fe/TiC} - (E_{bcc-Fe} + E_{TiC}) \right] / 2A \qquad (4)$$

where A is the interfacial area; Ebcc-Fe/TiC is the total energy of the interface; Ebcc-Fe and ETiC are the total energies of individual bcc-Fe
and TiC, respectively. However, Ebcc-Fe/TiC is closely related to the interfacial spacing. The appropriate interfacial spacing is determined by UBER (universal binding energy relation) method. Bcc-Fe/TiC interfacial models with various interfacial spacing (the longest dimension of the models also varied accordingly) are constructed and fully relaxed. Then the work of adhesion Wad is calculated as follow:

$$W_{ad} = \left[(E'_{bcc-Fe} + E'_{TiC}) - E_{bcc-Fe/TiC} \right] / 2A \qquad (5)$$

where E'bcc-Fe and E'TiC are the total energies of individual bcc-Fe and TiC models with free surfaces. Wad is defined as the reversible work of separating an interface into two pure substances with free surfaces. E'bcc-Fe and E'TiC are calculated by the relaxations of individual bcc-Fe and TiC models built by adding 30 Å thick vacuum in the z-direction. Similarly, the molecular statics merely allows full relaxations on the direction perpendicular to

the interfaces but maintain the same lattice parameters as the interfacial models in two directions parallel to the interfaces. Put the values of Ebcc-Fe/TiC with various interfacial spacing into Eq. (4) and the relationship between Wad and interfacial spacing can be obtained, which is shown in Fig. 4. It can be seen that the appropriate interfacial spacing for the three types of bcc-Fe/TiC interfaces are d0(type-1) ¼ 2.77 Å, d0(type-2) ¼ 2.47 Å and d0(type-3) ¼ 2.58 Å respectively. Put the values of Ebcc-Fe/TiC at these interfacial spacing into Eq. (3) and the interfacial energies are g(type-1) ¼ 0.29 J/m2, g(type-2) ¼ 3.41 J/m2 and g(type-3) ¼ 1.02 J/ m2 respectively, which are listed in Table 1. From thermodynamics perspective, the interface is more stable with lower interfacial energy and the cohesion is stronger with higher work of adhesion. Therefore, bcc-Fe/TiC interface is optimal with type-1 atomic stacking mode. J.H. Jang et al. [38] have also calculated the interfacial energy between bcc-Fe and TiC by first-principles. They only constructed one kind of interface with type-1 atomic stacking mode, and the interfacial energy (0.34 J/m2) is close to our result.

3.3. Interfacial electronic structure of bcc-Fe/TiC.

The interfacial electronic structure can be characterized by electron density and electron density difference. Figs. 5-7 show the interfacial electron densities and interfacial electron density differences of the three types of bcc-Fe/TiC interfaces, in which the dashed lines represent the interfaces and the upper districts are TiC while the lower districts are bcc-Fe. In the electron densities, the transition from blue to red represents charge density is gradually increased. In the electron density differences, the transition from blue to red represents the transition from charge depletion to charge accumulation and the white curves are the contour curves where charge is not changed.

Fig. 5 shows the electronic structure of type-1 interface on the (110)bcc_Fe plane perpendicular to the interface (namely (100)TiC plane). It can be seen from Fig. 5a that Fe atom and C atom form FeeC bond on the interface. From Fig. 5b, the obvious charge depletion of Fe atom and charge accumulation of C atom suggests the ionic characteristic of Fe-C bond. Together with the population of Fe-C bond is 0.48, it is polar covalent/ionic bond. In Fig. 5, the Ti and C atoms nearest to the interface are on the same plane originally. While the C atom moves 0.16 Å towards the interface with the action of Fe-C polar covalent/ionic bond, which suggests the interaction between Fe and C atoms is attractive. Because the distance between Fe and Ti atoms is far and the bonding is weak, the distance between them almost does not change.

Fig. 6 shows the electronic structure of type-2 interface on (110)bcc_Fe plane perpendicular to the interface (namely (100)TiC plane). It can be seen from Fig. 6a that Fe atom and Ti atom form Fe-Ti bond on the interface. From Fig. 6b, the charge of Fe atom and Ti atom transfers medially, which suggests the metallic characteristic of Fe-Ti bond. In Fig. 6, the Ti atom nearest to the interface moves 0.19 Å away from the interface with the action of Fe-Ti metallic bond, which suggests the interaction between Fe and Ti atoms is repulsive. Because the distance between Fe and C atoms is far and the bonding is weak, the distance between them almost does not change.

Fig. 7 shows the electronic structure of type-3 interface on different planes perpendicular to the interface. It can be seen from Fig. 7a and c that Fe-C bond and Fe-Ti bond are formed on the interface. From the electron density difference on (100)bcc_Fe plane (namely (110)TiC plane) in Fig. 7b, the charge of Fe atom is partially transferred to the bonded C atom. Combined with the nonzero population, the FeeC bond is polar covalent/ionic bond. From the electron density difference on (010)bcc_Fe plane (namely (110)TiC plane) in Fig. 7d, the medially

transferred charge of Fe atom and the bonded Ti atom suggests the metallic characteristic of Fe-Ti bond.

In Fig. 7, where the Ti and C atoms nearest to the interface are of the equivalent distance to the bonded Fe atoms originally, the C atoms move 0.21 Å towards the interface with the action of Fe-C polar covalent/ionic bonds. While the Ti atoms merely moves 0.02 Å away from the interface with the action of Fe-Ti metallic bonds, which suggests the attractive interaction between Fe and C atoms is stronger than the repulsive interaction between Fe and Ti atoms. From the electronic structures as well as the works of adhesion and interfacial energies, the interface combined by Fe-C polar covalent/ionic bond is more stable than that combined by Fe-Ti metallic bond. Besides, adhesion by Fe-C polar covalent/ionic bond is stronger than that by Fe-Ti metallic bond.

3.4. Solid-liquid interfacial energy of bcc-Fe

3.4.1. Melting point

The bcc-Fe supercell system sized 40 x 40 x 40 (containing 128000 Fe atoms) is built within a box with the size Lx-Ly-Lz of 11.48 nm-11.48 nm-11.48 nm, whose side surfaces are parallel to the {001} family. The system reaches equilibrium at 1000 K and then is slowly heated to the equilibrium at 3500 K. Fig. 8 shows the relationship of equilibrium energies versus temperature during the heating process. From 1000 K to 2092K, the energy varies linearly with the increasing temperature, namely the curve in this range reflects the energy change of the bcc-Fe crystal. The slope of the curve suddenly changes at 2092K, which suggests the transformation from crystal state to molten state. Therefore, the melting point Tm of bcc-Fe is 2092K. Y. Shibuta et al. [39] have estimated the melting point of bcc-iron as 2400 K from the temperature at which the system with coexisting solid and liquid by using Finnis-Sinclair (FS) potential. The measured melting point of ferritic stainless steel is about 1800 K [40]. Our calculation error falls within a more reasonable range compared to Y. Shibuta's result [39]. While there is still a difference between the measured and calculated melting point, which may be due to the fact that ferritic stainless steel contains other elements such as Cr and these elements may change the melting point of ferrite.

3.4.2. Solid-liquid interfacial energy

According to the classical nucleation theory [41], an undercooling degree DT is necessary for the solidification of metal whose solid-liquid interface is of curvature. This phenomenon is the so called Gibbs-Thomson effect. The expression of Gibbs-Thomson effect is given as follow:

$$\Delta T = \Gamma K, \quad K = \frac{1}{r_1} + \frac{1}{r_2} \qquad (5)$$

where Γ is the Gibbs-Thomson coefficient; K is the curvature of the embryo; r1 and r2 are the radii of curvature, respectively. For a sphere embryo, K ¼ 2r . Thereby:

$$\Delta T = \Gamma \frac{2}{r} \qquad (6)$$

Gibbs-Thomson coefficient can be obtained by the following equation:

$$\Gamma = \frac{\gamma_{SL}}{\Delta S} \qquad (7)$$

$$\Delta S = \frac{\rho_S}{T_m} \Delta H \qquad (8)$$

where γ_{SL} is the solid-liquid interfacial energy; ρ_S is the number density of bcc-Fe crystal; ΔH is the melting enthalpy at Tm. ρ_S =8:46e28 atom/m^3 of bcc-Fe can be obtained from its lattice parameter and number of atoms in a unit cell. The value of ΔH can be obtained in the following way. Firstly, the system reaches equilibrium at Tm to acquire the total energy of bcc-Fe crystal. Secondly, the system is kept at 3000 K and then kept at Tm to acquire the total energy of bcc-Fe melt. Finally, ΔH= 1.5x10^{-20}atom is obtained. Put the values of ρS, ΔH and Tm into Eq. (8) and ΔS=6:07e5 j/k m^3 can be gotten. Based on Eq. (7), γSL can be obtained if Γ is known. From Eq. (6), Γ can be known from the relationship between ΔT and r.

The relationship between ΔT and r can be obtained in the following way. Firstly, the system is kept at Tm until it reaches energy equilibrium and then the coordinates of the atoms in the sphere region with radius R in the center are fixed. Then the system is kept at 2500 K until the atoms except those in the sphere region reach molten state. By this means, an embryo with critical radius R embedded in the bcc-Fe melt is constructed, which is schematically displayed in Fig. 9. According to the classical nucleation theory [41], if ΔT is lower than the critical undercooling degree ΔT^*, the embryo will melt; otherwise the embryo will grow. Therefore, we set free the atoms in the sphere region and rapidly apply a ΔT to the system (namely rapidly cool the system to a certain degree which is lower than Tm). Numerous ΔT are applied until the radius of the embryo just do not change, namely ΔT^* for the embryo is reached. During the calculation process, the characterization of the radius is of vital importance. The coordination number (number of the nearest atoms) of atom in bcc-Fe crystal is 8, while that in bcc-Fe melt is not a constant value. The coordination numbers of each atom after rapid cooling are analyzed. The atoms in the center with coordination number equals 8 are identified as bcc-Fe crystal so that the radius of the embryo is determined. Numerous calculations with different radii are performed and the relationship between ΔT^* and R is obtained, which is displayed in Fig. 10. The fitting line of the resultant points is as follow:

$$\Delta T = 6 \times 10^{-7} \frac{2}{R} \qquad (9)$$

atomic stacking mode, which is combined by Fe-C polar covalent/ionic bonds. The interfacial energy of type-1 interface is 0.29 J/m2, which is lower than the solid-liquid interfacial energy of bcc-Fe (0.36 J/m2). Based on the classical nucleation theory [16], it means TiC can act as the heterogeneous nucleus of bcc-Fe, which reveals the refinement mechanism of ferrite with TiC particles. The solid-liquid interfacial energy can be measured by experimental methods [42]. However, it is still impossible to completely eradicate the influence of heterogeneous nucleus, namely measurement without any foreign impurity is still unfulfilled, which leads to the large error in the solid-liquid interfacial energy under homogeneous nucleation circumstance. Instead, molecular statics/dynamics can simulate homogeneous nucleation behavior without any foreign impurity. Combining molecular statics/dynamics with first-principles, the theoretic basis of TiC as the heterogeneous nucleus of ferrite is fundamentally explained.

4. Conclusions

(1) Bcc-Fe/TiC interfaces with different atomic stacking modes are constructed and then calculated by molecular statics. The works of adhesion and interfacial energies are associated with the atomic stacking modes. The works of adhesion are 4.13 J/m^2 (type-1), 1.01 J/m^2 (type-

2) and 3.41 J/m^2 (type-3) respectively. The interfacial energies are 0.29 J/m^2 (type-1), 3.41 J/m^2 (type-2) and 1.02 J/m^2 (type-3) respectively.

(2) The interfacial electronic structures of the bcc-Fe/TiC interfaces are analyzed by first-principles. Type-1 interface is combined by Fe-C polar covalent/ionic bonds, which result in the attractive interaction between Fe and C atoms. Type-2 interface is combined by Fe-Ti metallic bonds, which result in the repulsive interaction between Fe and Ti atoms. Type-3 interface is combined by FeeC polar covalent/ionic bonds and Fe-Ti metallic bonds, and the former are stronger than the later.

(3) The solid-liquid interfacial energy γSL of bcc-Fe calculated by molecular dynamics is 0.36 J/m^2. Based on the classical nucleation theory, the interfacial energy of bcc-Fe/TiC type-1 interface is lower than the solid-liquid interfacial energy of bcc-Fe, which means TiC can act as the heterogeneous nucleus of bcc-Fe and thereby refines it.

References
[1] K.H. Lo, C.H. Shek, J.K.L. Lai, Recent developments in stainless steels, Mater. Sci. Eng. R 65 (2009) 39-104.
[2] H. Takeughi, H. Mori, Y. Ikehara, T. Komano, T. Yanai, The effects of electromagnetic stirring on cast structure of continuously cast SUS430 stainless steel slabs, ISIJ 66 (1980) 638-646.
[3] Y.D. Wu, Y.H. Cai, X.H. Chen, T. Wang, J.J. Si, L. Wang, Y.D. Wang, X.D. Hui, Phase composition and solid solution strengthening effect in TiZrNbMoV high-entropy alloys, Mater. Des. 83 (2015) 651-660.
[4] B. Gwalani, V. Soni, M. Lee, S.A. Mantri, Y. Ren, R. Banerjee, Optimizing the coupled effects of Hall-Petch and precipitation strengthening in a Al0.3CoCr-FeNi high entropy alloy, Mater. Des. 121 (2017) 254-260.
[5] Y.B. Miao, K. Mo, Z.J. Zhou, X. Liu, K.C. Lan, G.M. Zhang, J.S. Parka, J. Almer, J.F. Stubbins, Mater. Des. 111 (2016) 622-630.
[6] K.C. Han, G.Q. Lin, C. Dong, K.P. Tai, X. Jiang, Experimental study on atomic scale strengthening mechanism of the IVB transition-metal nitrides, J. Alloys Compd. 696 (2017) 572-579.
[7] W.B. Guo, T.M. Luan, J.S. He, J.C. Yan, Ultrasonic-assisted soldering of fine grained 7034 aluminum alloys using ZnAl filler metals, Mater. Des. 125 (2017) 85-93.
[8] Z.W. Yu, A.T. Tang, Q. Wang, Z.Y. Gao, J.J. He, J. She, K. Song, F.S. Pan, High strength and superior ductility of an ultra-fine grained magnesiummanganese alloy, Mater. Sci. Eng. A 648 (2015) 202-207.
[9] M. Samaee, S. Najafi, A.R. Eivani, H.R. Jafarian, J. Zhou, Simultaneous improvements of the strength and ductility of fine-grained AA6063 alloy with increasing number of ECAP passes, Mater. Sci. Eng. A 669 (2016) 350-357.
[10] C.X. Shi, G.G. Cheng, Z.J. Li, P. Zhao, Solidification structure refining of 430 ferrite stainless steel with TiN nucleation, J. Iron Steel Res. Int. 15 (2008)

57-60.

[11] S.M. Hong, E.K. Park, J.J. Park, M.K. Lee, J.G. Lee, Effect of nano-sized TiC particle addition on microstructure and mechanical properties of SA-106B carbon steel, Mater. Sci. Eng. A 643 (2015) 37-46.

[12] M.K. Lee, E.K. Park, J.J. Park, C.K. Rhee, A nanoscale dispersion of TiC in cast carbon steel through a reaction in melt, Mater. Chem. Phys. 138 (2013) 423-426.

[13] A.O. Titov, R. Inoue, H. Suito, Grain-growth-inhibiting effects of TiC and ZrC precipitates in Fee0.15~0.30mass%C alloy, ISIJ Int. 48 (2008) 301-309.

[14] Y. Kang, W.M. Mao, Y.J. Chen, J. Jing, M. Cheng, Effect of Ti content on grain size and mechanical properties of UNS S44100 ferritic stainless steel, Mater. Sci. Eng. A 677 (2016) 211-221.

[15] Y. Kang, W.M. Mao, Y.J. Chen, J. Jing, M. Cheng, Influence of Nb content on grain size and mechanical properties of 18wt%Cr ferritic stainless steel, Mater. Sci. Eng. A 677 (2016) 453-464.

[16] T. Iwasaki, A. Matsuyama, H. Nakamura, S. Watano, Rapid synthesis of octosilicate, a layered alkali silicate, by heterogeneous nucleation at the solid liquid interface, Appl. Clay Sci. 58 (2012) 39-43.

[17] X.J. Wu, J.D. Xing, H.G. Fu, X.H. Zhi, Effect of titanium on the morphology of primary M7C3 carbides in hypereutectic high chromium white iron, Mater. Sci. Eng. A 457 (2007) 180-185.

[18] S. Kou, Welding Metallurgy, second ed., John Wiley, Hoboken, 2003.

[19] T. Yuan, S. Kou, Z. Luo, Grain refining by ultrasonic stirring of the weld pool, Acta Mater. 106 (2016) 144-154.

[20] S.X. Jin, N. Liu, S. Zhang, D. Li, The simulation of interface structure, energy and electronic properties of TaN/ReB2 multilayers using first-principles, Surf. Coat. Technol. 326 (2017) 417-423.

[21] J. Li, M. Zhang, Y. Zhou, G.X. Chen, First-principles study of Al/A13Ti heterogeneous nucleation interface, Appl. Surf. Sci. 307 (2014) 593-600.

[22] A.C. Silva, J. Agren, M.T. Clavaguera-Mora, D. Djurovic, T. Gomez-Acebo, B.J. Lee, Z.K. Liu, P. Miodownik, H.J. Seifert, Applications of computational thermodynamics-the extension from phase equilibrium to phase transformations and other properties, Calphad 31 (2007) 53-74.

[23] Y. Shibuta, S. Sakane, T. Takaki, M. Ohno, Submicrometer-scale molecular dynamics simulation of nucleation and solidification from undercooled melt: linkage between empirical interpretation and atomistic nature, Acta Mater. 105 (2016) 328-337.

[24] P.B. Zhang, J.H. Ding, D. Sun, J.J. Zhao, First-principles study of noble gas atoms in bcc Fe, J. Nucl. Mater. 492 (2017) 134-141.

[25] T. Ohnuma, N. Soneda, M. Iwasawa, First-principles calculations of vacancysolute element interactions in body-centered cubic iron, Acta Mater. 57 (2009) 5947-5955.

[26] B.J. Lee, J.W. Lee, A modified embedded atom method interatomic potential for carbon, Calphad 29 (2005) 7-16.

[27] B.J. Lee, T.H. Lee, S.J. Kim, A modified embedded-atom method interatomic potential for the Fe-N system: a comparative study with the Fe-C system, Acta Mater. 54 (2006) 4597-4607.

[28] B.J. Lee, A modified embedded-atom method interatomic potential for the Fe-C system, Acta Mater. 54 (2006) 701-711.

[29] M.I. Mendelev, S. Han, D.J. Srolovitz, G.J. Ackland, D.Y. Sun, M. Asta, Development of new interatomic potentials appropriate for crystalline and liquid iron, Philos. Magn. A 83 (2003) 3977-3994.

[30] W.B. Pearson, A Hand Book of Lattice Spacings and Structure of Metals and Alloys, vol. 2, Pergamon Press, London, 1967, p. 908.

[31] Y.F. Yang, H.Y. Wang, J. Zhang, R.Y. Zhao, Y.H. Liang, Q.C. Jiang, Lattice parameter and stoichiometry of TiCx produced in the Ti-C and Ni-Ti-C systems by self-propagating high-temperature synthesis, J. Am. Ceram. Soc. 91 (2008) 2736-2739.

[32] R. Okamoto, A. Borgenstam, J. Ågren, Interphase precipitation in niobiummicroalloyed steels, Acta Mater. 58 (2010) 4783-4790.

[33] H.W. Yen, C.Y. Chen, T.Y. Wang, C.Y. Huang, J.R. Yang, Orientation relationship transition of nanometre sized interphase precipitated TiC carbides in Ti
bearing steel, Mater. Sci. Technol. 26 (2010) 421-430.

[34] H.W. Yen, C.Y. Huang, J.R. Yang, Characterization of interphase-precipitated nanometer-sized carbides in a Ti-Mo-bearing steel, Scr. Mater. 61 (2009)
616-619.

[35] H.W. Yen, P.Y. Chen, C.Y. Huang, J.R. Yang, Interphase precipitation of nanometer-sized carbides in a titanium-molybdenum-bearing low-carbon steel, Acta Mater. 59 (2011)
6264-6274.

[36] M.Y. Chen, H.W. Yen, J.R. Yang, The transition from interphase-precipitated carbides to fibrous carbides in a vanadium-containing medium-carbon steel,
Scr. Mater. 68 (2013) 829-832.

[37] A.C. Silva, J. Agren, M.T. Clavaguera-Mora, D. Djurovic, T. Gomez-Acebo, B.J. Lee, Z.K. Liu, P. Miodownik, H.J. Seifert, Applications of computational
thermodynamics-the extension from phase equilibrium to phase transformations and other properties, Calphad 31 (2007) 53-74.

[38] J.H. Jang, C.H. Lee, Y.U. Heo, D.W. Suh, Stability of (Ti,M)C (M¼Nb, V, Mo and W) carbide in steels using first-principles calculations, Acta Mater. 60 (2012)
208-217.

[39] Y. Shibuta, S. Takamoto, T. Suzuki, A molecular dynamics study of the energy and structure of the symmetric tilt boundary of iron, ISIJ Int. 48 (2008)
1582-1591.

[40] T.J. Tanaka, B. Smith, K.P. Troncosa, Ferritic Steel Melt and FLiBe/steel Experiment, 2004.

[41] W. Kurz, D.J. Fisher, Fundamental of Solidification, fourth ed., Trans Tech Publication, Aedermannsdorf, 1998.

[42] D. Turnbull, Formation of crystal nuclei in liquid metals, J. Appl. Phys. 21 (1950) 1022-1028.

Table 1
W_{ad} and γ of bcc-Fe/TiC interfaces by molecular statics.

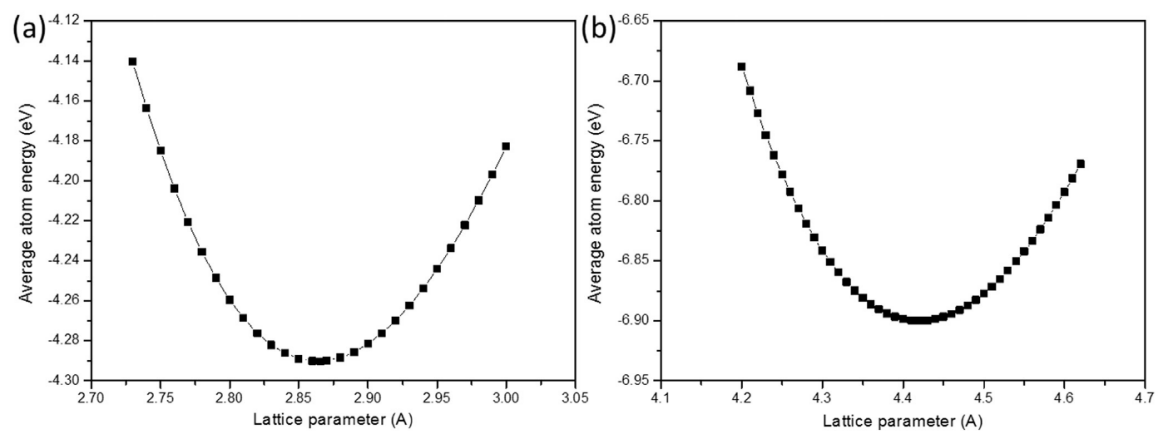| Type	Work of adhesion (J/m^2)	Interfacial energy (J/m^2)
1	4.13	0.29
2	1.01	3.41
3	3.41	1.02

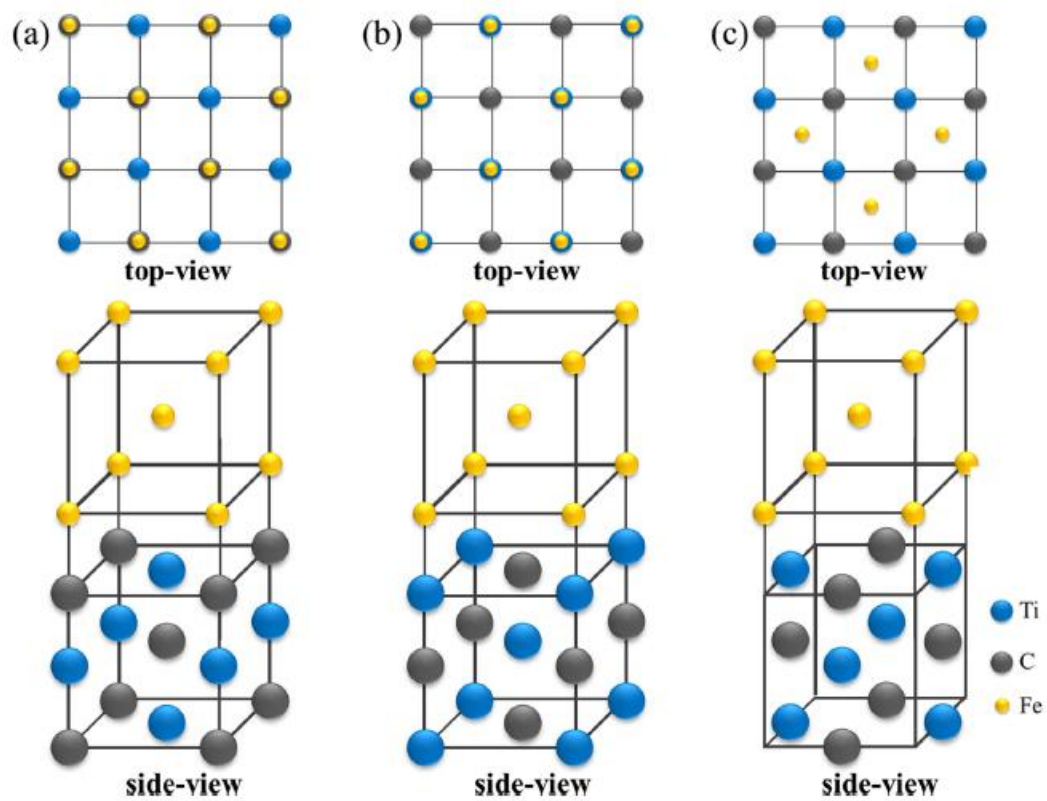Fig. 1. Relationship of equilibrium energies versus lattice parameters. (a) bcc-Fe; (b) TiC.

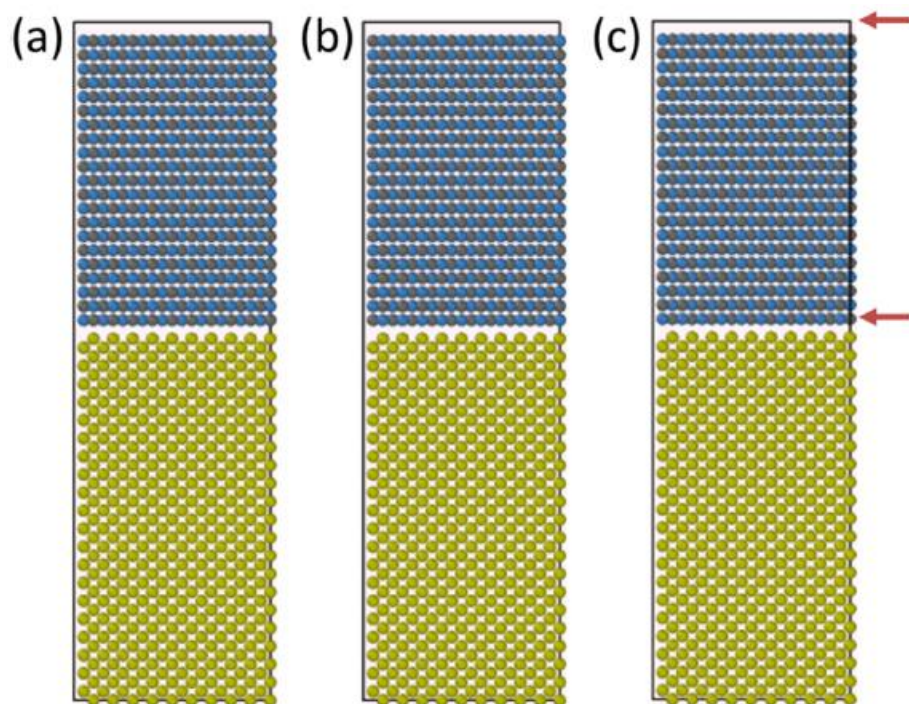Fig. 2. Schematic diagrams of bcc-Fe/TiC interfaces. (a) Type-1; (b) type-2; (c) type-3.

Fig. 3. Left views (seen from positive x-direction) of the interfacial models. (a) Type-1; (b) type-2; (c) type-3.
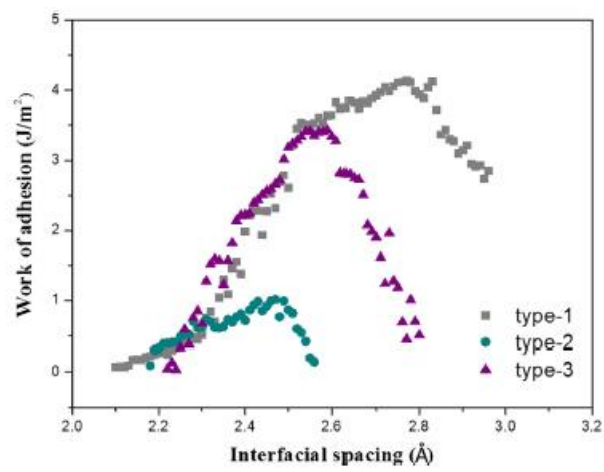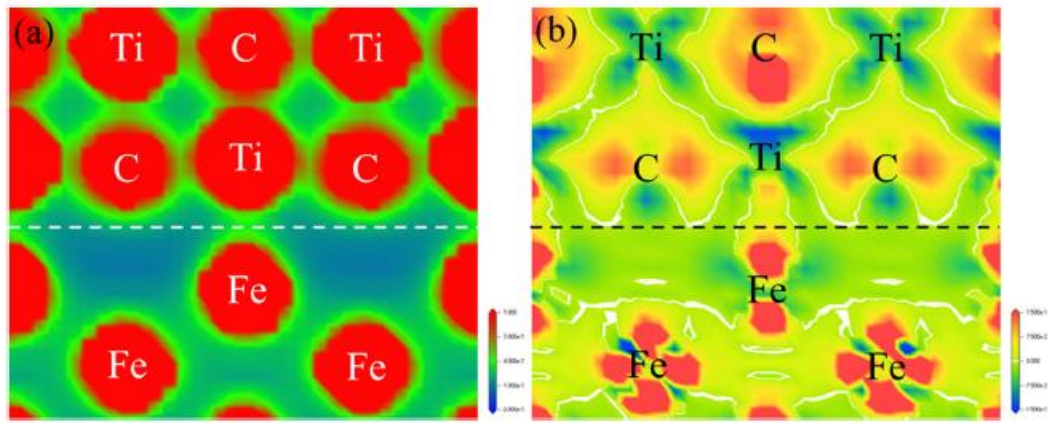
Fig. 4. Relationship between Wad and interfacial spacing.
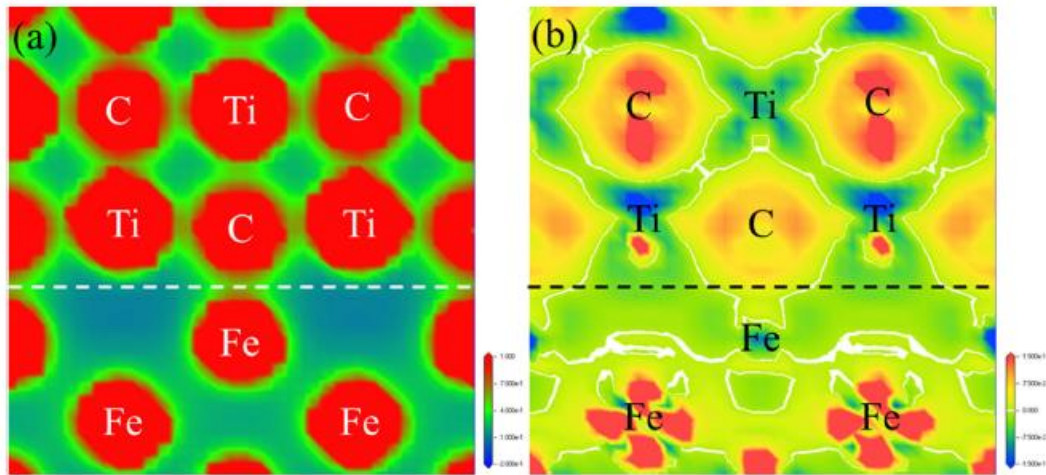
Fig. 5. Electronic structure of type-1 interface on the (110)$_{bcc\_Fe}$ plane perpendicular to the interface (namely ð100ÞTiC plane). (a) Electron density; (b) electron density difference.

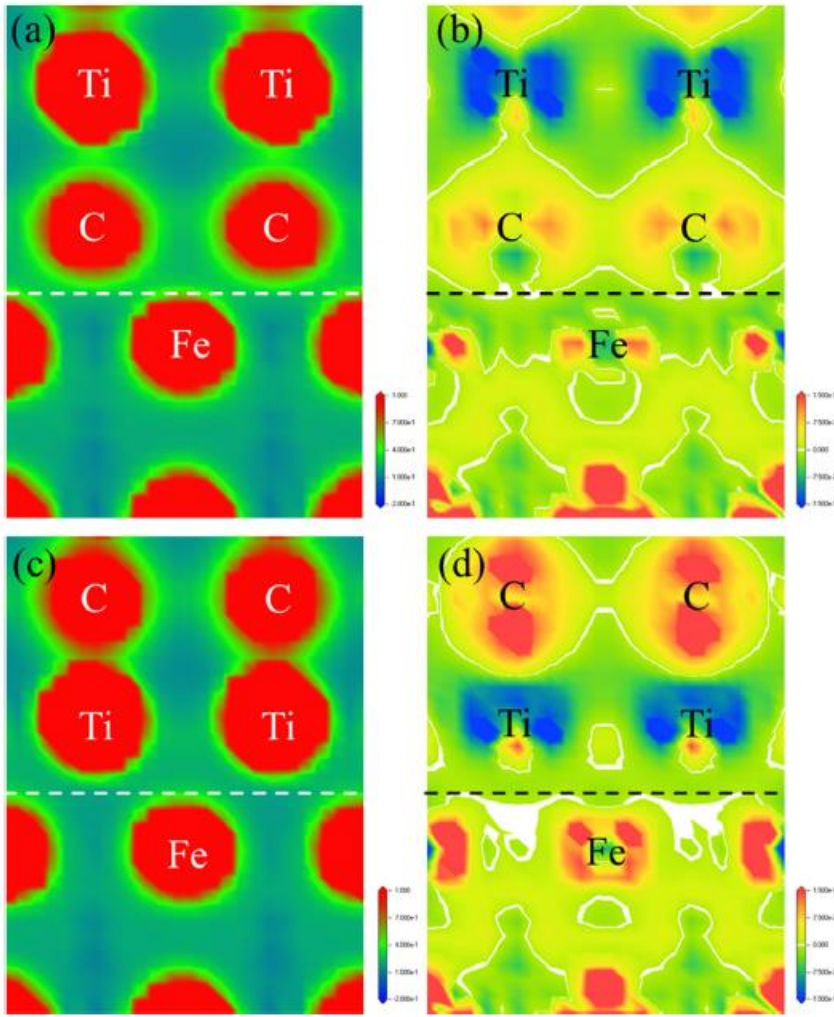Fig. 6. Electronic structure of type-2 interface on the (110)$_{bcc\_Fe}$ plane perpendicular to the interface (namely (100)$_{TiC}$ plane). (a) Electron density; (b) electron density difference.

Fig. 7. Electronic structure of type-3 interface. (a) Electron density and (b) electron density difference on the (100)$_{bcc\_Fe}$ plane perpendicular to the interface (namely (110)$_{TiC}$ plane). (c) Electron density and (b) electron density difference on the (010)$_{bcc\_Fe}$ plane perpendicular to the interface (namely (110)$_{TiC}$ plane).
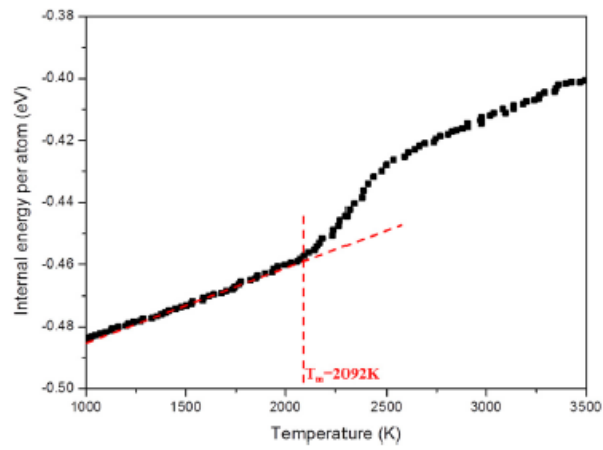
Fig. 8. Relationship of bcc-Fe equilibrium energies versus temperature during the heating process.
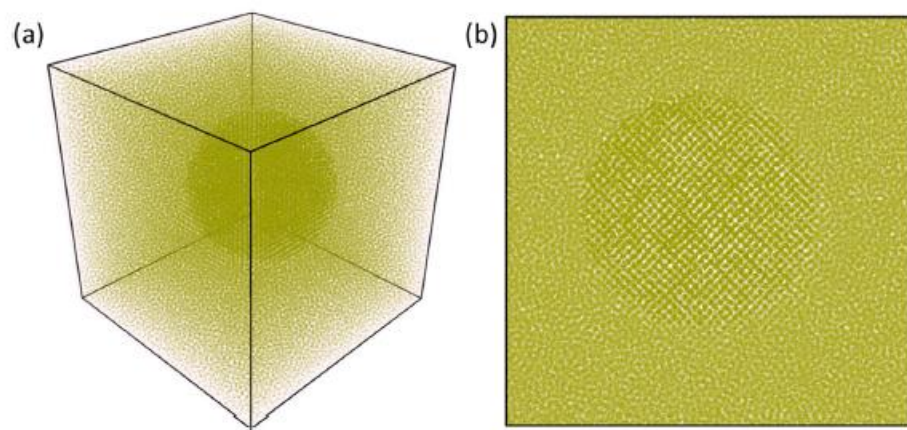
Fig. 9. Schematic diagram of an embryo with critical radius R embedded in the bcc-Fe melt. (a) 3-dimensional view; (b) side view.
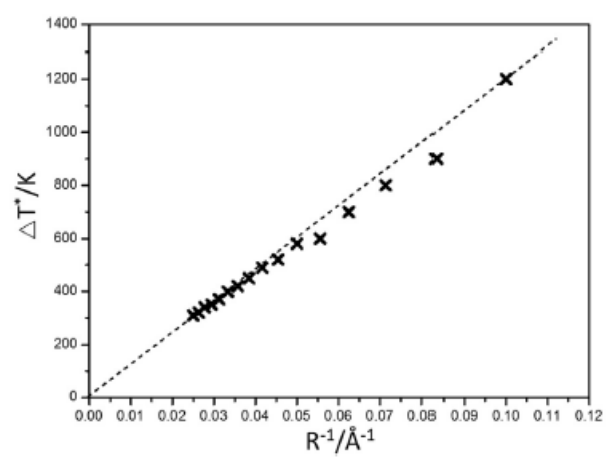
Fig. 10. Relationship between ΔT^{*} and R.